

Propagating Disturbances in Coronal Loops: A Detailed Analysis of Propagation Speeds

G. Kiddie¹ · I. De Moortel¹ · G. Del Zanna² ·
S.W. McIntosh³ · I. Whittaker¹

© Springer

Abstract Quasi-periodic disturbances have been observed in the outer solar atmosphere for many years. Although first interpreted as upflows (Schrijver *et al.* Solar Physics.187,261), they have been widely regarded as slow magneto-acoustic waves, due to their observed velocities and periods. However, recent observations have questioned this interpretation, as periodic disturbances in Doppler velocity, line width, and profile asymmetry were found to be in phase with the intensity oscillations (De Pontieu and McIntosh, Astrophysics. J. 722,1013 (2010), Tian, McIntosh, and De Pontieu, Astrophysics, J.Lett. 727,L37 (2011)), suggesting that the disturbances could be quasi-periodic upflows. Here we conduct a detailed analysis of the velocities of these disturbances across several wavelengths using the *Atmospheric Imaging Assembly* (AIA) onboard the *Solar Dynamics Observatory* (SDO). We analysed 41 examples, including both sunspot and non-sunspot regions of the Sun. We found that the velocities of propagating disturbances (PDs) located at sunspots are more likely to be temperature dependent, whereas the velocities of PDs at non-sunspot locations do not show a clear temperature dependence. This suggests an interpretation in terms of slow magneto-acoustic waves in sunspots but the nature of PDs in non-sunspot(plage) regions remains unclear. We also considered on what scale the underlying driver is affecting the properties of the PDs. Finally, we found that removing the contribution due to the cooler ions in the 193 Å wavelength suggests that a substantial part of the 193 Å emission of sunspot PDs can be attributed to the cool component of 193 Å.

Keywords: Oscillations, Corona, Waves, Flows, Velocities

¹ School of Mathematics and Statistics, University of St Andrews, North Haugh, St Andrews, Fife, KY16 9SS, Scotland, UK. gregk@mcs.st-and.ac.uk
ineke@mcs.st-and.ac.uk email: icw@mcs.st-and.ac.uk ²
Department of Applied Mathematics and Theoretical Physics, Wilberforce Road, Cambridge, CB30WA
email:G.Del-Zanna@damtp.cam.ac.uk ³ High Altitude Observatory, National Center for Atmospheric Research, P.O. Box 3000, Boulder, CO 80307 email: mscott@ucar.edu

1. Introduction

Since the launch of SOHO and TRACE, low-amplitude quasi-periodic disturbances have been found at loop foot points (*e.g.* De Moortel (2009) for a review). The first observations of propagating disturbances (PDs) were found along coronal plumes by Ofman *et al.* (1997) using SOHO/UVCS, and again by Deforest and Gurman (1998) using SOHO/EIT. These were observed as intensity perturbations travelling at approximately the local sound speed. This led to their classification as slow magneto-acoustic waves (see reviews by De Moortel (2009) and Banerjee, Gupta, and Teriaca (2011)). Propagating disturbances of a similar nature (in active region loops) were observed by Berghams and Clette (1999) using SOHO/EIT. Schrijver *et al.* (1999), Nightingale, Aschwanden, and Hurbert (1999), De Moortel, Ireland, and Walsh (2000) found similar disturbances using TRACE, while Berghams, McKenzie, and Clette (2001) found them using *Yokhoh*/SXT. These perturbations usually have small amplitudes of the order of a few percent of the background. They were found to have velocities of approximately 100 km s^{-1} and periods of two–ten minutes (McEwan and De Moortel, 2006). There has also been substantial work done in theoretical modelling of these disturbances (Nakariakov *et al.*, 2000; Tsiklauri and Nakariakov, 2001; De Moortel and Hood, 2004; De Moortel *et al.*, 2004). These authors have looked at a variety of aspects under the assumption that these disturbances are slow magneto-acoustic waves and found that the observed amplitude decay could be explained in terms of thermal conduction. The quasi-periodic nature of these waves has been attributed to the leakage of *p*-modes into the solar atmosphere (De Pontieu, Erdélyi, and De Moortel, 2005; De Moortel and Rosner, 2007; Malins and Erdélyi, 2007). Marsh and Walsh (2009) inferred a coronal temperature using EIS and found a temperature that agrees with the seismologically calculated temperature found by Marsh, Walsh, and Plunkett (2009). They suggested that this agrees with the interpretation of the disturbances as slow magneto-acoustic waves.

Although this interpretation was widely accepted for several years, in the last few years it has been questioned again, as spectroscopic observations from *Hinode*/EIS have shown the situation is not so straightforward. These observations still show quasi-periodic intensity perturbations which are correlated (*i.e.* in phase) with perturbations in Doppler velocity, line width, and line asymmetry. This has led to an alternative interpretation as high-velocity upflows as this coherent behaviour is hard to explain with a slow wave scenario (De Pontieu and McIntosh, 2010; Tian, McIntosh, and De Pontieu, 2011; Nishizuka and Hara, 2011). Sakao *et al.* (2007) found faint up flows in spectra of transition-region and coronal-loop foot points. De Pontieu *et al.* (2009) discovered that these up flows are ubiquitous in foot points of coronal loops. A link between small blue-ward asymmetries in spectra of loop foot points and the propagating disturbances was found (De Pontieu and McIntosh, 2010; Tian, McIntosh, and De Pontieu, 2011; Tian *et al.*, 2011). These were found by fitting the lines with a double Gaussian model and using a red-blue asymmetry analysis (De Pontieu and McIntosh, 2010; Tian *et al.*, 2011; Bryans, Young, and Doschek, 2011). Other studies that use the interpretation as flows include Doschek *et al.* (2007), De Zanna

(2008), He *et al.* (2010), Peter (2010), Harra *et al.* (2008), Warren *et al.* (2011), Marsch (2008), Hara *et al.* (2008), Tian *et al.* (2011), Murray *et al.* (2010), Brooks and Warren (2011), and Young, O’Dwyer, and Mason (2012). This has not closed the debate though. Verwichte *et al.* (2010) showed that these periodic line asymmetries could be explained by slow magneto-acoustic waves. There are many other studies that still show a preference for the slow wave interpretation (Marsh, Walsh, and Plunkett, 2009; Wang, Ofman, and Davila, 2009; Kitagawa *et al.*, 2010; Banerjee *et al.*, 2009; Mariska and Muglach, 2009; Krishna Prasad, Banerjee, and Gupta, 2011). It has been suggested that these PDs can have a close connection with type II spicules (De Pontieu *et al.*, 2009; De Pontieu *et al.*, 2011; Rouppe van der Voort, 2011) and they have also been linked with the mass cycle of the solar wind (McIntosh *et al.*, 2010; Tian *et al.*, 2011). Due to their ubiquitous nature, they could have a significant effect on the coronal energy budget. Recent work by McIntosh *et al.* (2012) shows a slow, downflow of coronal material, which could be the return component of the up flow. Other articles that consider downflows include Kamio *et al.* (2011) and Ugarte-Urra and Warren. (2011).

This so called “Flows versus Waves” debate has been argued for several years now, with a definitive answer yet to be decided (if there is one). In this article we study propagating disturbances found at loop foot points, using the *Atmospheric Imaging Assembly* (AIA) onboard the *Solar Dynamics Observatory* (SDO). We are going to look at the velocities of these disturbances over a range of different wavelengths and temperatures. We are going to consider the velocities of these disturbances in different bands, which are dominated by lines formed in a range of temperatures (O’Dwyer *et al.* (2010), De Zanna, O’Dwyer, and Mason (2011)). In particular, we consider the 131, 171, and 193 Å bands. As shown by Del Zanna *et al.* (2011), for the active-region loops considered here, these three bands are dominated by Fe VIII, Fe IX, and a range of ions (Fe VII–Fe XII) respectively. In ionisation equilibrium, these three bands show emission from plasma formed in a broad range of temperatures, centred around 0.4, 0.7, and 1.6 MK (Dere *et al.*, 2009). The other AIA bands are more multi-thermal or lack atomic data (De Zanna, O’Dwyer, and Mason, 2011).

The outline of this article is as follows: Section 2 describes the two primary data sets studied in this article. Section 3 describes how the velocities of the observed PDs change with temperature by looking at 131, 171, and 193 Å observations of both data sets. A description of how the properties of the PDs change across an active region is described in Section 4. In Section 5 we describe a method to remove the contribution due to cool ions in the 193 Å passband and the effect this has on the properties of the observed PDs. The discussion and conclusions are presented in Section 6.

2. Observations and Analysis

The two primary data sets investigated are AIA observations of active regions AR11236 on 22 June 2011 at 15:13UT and AR11301 on 22 September 2011 at 15:01UT. Both data sets have a duration of 40 minutes. We will focus on the

131,171, and 193 Å passbands. Each passband has a cadence of 12 seconds and exposure times of 2.9, 2.0, and 2.0s respectively. Each data set has been cleaned and co-aligned using the SolarSoft IDL command `AIA_PREP` and these are then de-rotated.

For each example a 150×150 pixel subsection is chosen to contain a loop footpoint. A loop is then outlined by two arcs, and divided into cross sections. This is a very similar technique to that of De Moortel, Ireland, and Walsh (2000). Consecutive images are summed to increase the signal to noise ratio and then we calculate a running-difference by subtracting from each image the one taken 96s previously. This is done to highlight the oscillations since we expect their periods to be approximately three–5 minutes.

3. Propagation Speeds In Multiple Wavelengths

In this section we look at the two data sets outlined in Section 2. We identify a loop and then create running-difference images to identify PDs along this loop. If the PDs are slow magneto-acoustic waves then their velocity is expected to be the local sound speed. The sound speed scales with temperature in the following way; $c_s^2 = \gamma \frac{p}{\rho}$ and $p = \frac{\rho k_B T}{\mu_m}$, and hence $c_s^2 = \alpha T$. The constant is defined as $\alpha = \gamma \frac{k_B}{\mu_m}$, where k_B is the Boltzmann constant and μ_m is the reduced mass, *i.e.* the average mass of all particles in the plasma. Therefore, the slow-wave propagation speed (which is closely related to the sound speed) is expected to be proportional to the square root of the temperature.

3.1. 22 September 2011 [Non Sunspot]

The first AIA observation is of active region AR11301 on 22 September 2011 as described in Section 2. The two arcs that outline the strands are shown on the top-left plot of Figure 1. The loop has solar coordinates of (-670,204) arcseconds at 00.35UT. To visualise the oscillations, a running-difference is made by subtracting the image 96 seconds earlier from each image. The running-difference images are shown in Figure 1(b)–(d) for the three different wavelengths. The overplotted lines in the running-difference images (b)–(d) represent the gradient of the intensity bands estimated in the 193 Å passband. They are overplotted as a visual aid to compare velocities of the PDs across the three wavelengths.

The velocities of the PDs are calculated from the inverse of the gradient of the intensity bands. For this example we identified five intensity bands in each wavelength and calculated a range of velocities as in De Moortel, Ireland, and Walsh (2000); the range of possible velocities is estimated from the range of slopes within a given intensity band. The velocities are displayed in Table 1. Band 1 is the intensity band closest to the bottom of the running-difference images and band 5 is closest to the top.

From Table 1 it is clear that the velocities of the PDs do not vary drastically across the wavelengths, with the largest range across wavelengths only 23 km s^{-1} . To gain a greater insight in how the PDs in each wavelength are related, we take cuts at fixed positions along the loop. Note that we have subtracted an eight

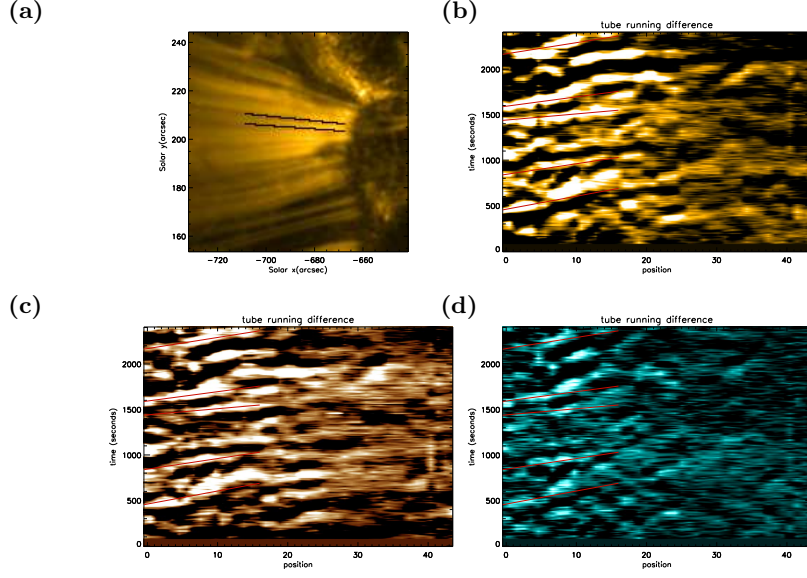


Figure 1. (a) 171 Å intensity image with the analysed loop outlined by the black lines. (b) – (d) Running-difference images for the 171 Å, 193 Å, and 131 Å passbands, respectively. The red lines correspond to the gradient of the intensity bands from the 193 Å running-difference.

Table 1. Average velocities associated with running-difference for all wavelengths (in km s^{-1}) for 22 September 2011. The velocities in the brackets show the lower and higher estimates.

Band	131 Å	171 Å	193 Å
1	48(27 – 190)	31(24 – 43)	49(34 – 90)
2	71(41 – 243)	63(39 – 128)	47(30 – 113)
3	86(53 – 228)	72(43 – 216)	82(44 – 533)
4	43(29 – 87)	36(26 – 56)	63(37 – 261)
5	42(29 – 75)	43(27 – 103)	50(35 – 87)

minute running average from the intensities to highlight the PDs as in Tian *et al.* (2011), which implies that periods greater than eight minutes will be suppressed. The PDs are no longer distinguishable by approximately position 12 along the loop, so we have taken cuts at position 1, 3, 5, and 7, which are displayed in Figure 2.

The black solid lines in Figure 2 correspond to cuts through the 171 Å intensity, the orange dashed lines are cuts through 193 Å and the blue dotted lines 131 Å. It should be noted that the 193 Å (orange dashed) and the 131 Å (blue dotted) lines have been multiplied by arbitrary constants to make them comparable in size to the 171 Å (black solid) line. In this figure, (a) shows cuts at position 1, which is near the bottom of the loop, (b) shows position 3, (c)

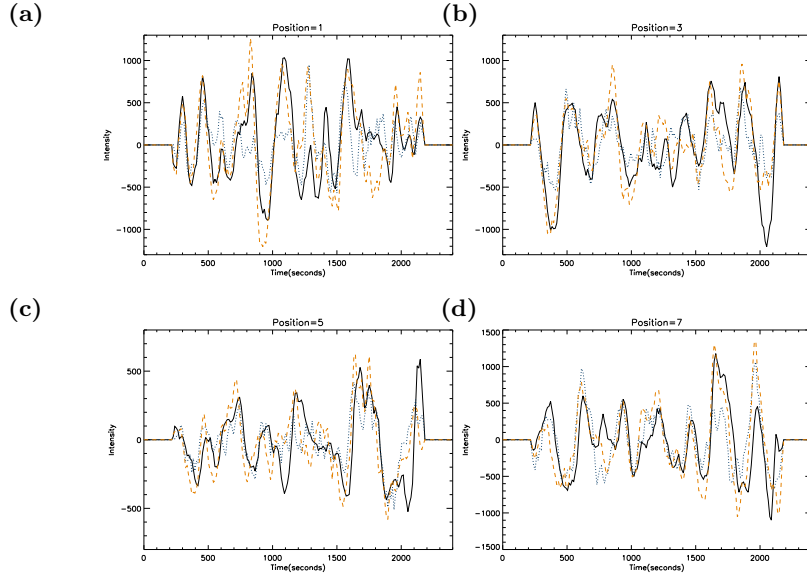


Figure 2. Cuts through the intensities for 171 Å (black solid), 193 Å (orange dashed) and 131 Å (blue dotted) for different positions along the tube, for 22 September 2011.

position 5, and (d) position 7. The three lines match well at position 1; the 193 Å and 171 Å lines are almost exactly in phase for the entire time with the 131 Å line also in phase for the majority of the time. This trend continues into positions 3 and 5. At position 7 the three lines are still approximately in phase although less so.

The final analysis we will use on this example is to consider a contour plot of the 193 Å running-difference with the 131 Å contours overplotted. Figure 3 shows this contour plot for a subsection of the running-difference images shown in Figure 1. It is clear from Figure 3 that the 131 Å contours match the 193 Å contours quite well. The rough shapes of the bands are well outlined by the 131 Å contours and the gradient of the bands are approximately the same.

The analysis performed on this data set suggests that the velocities of the PDs do not change considerably with the temperature and do not show the temperature dependence expected for a slow magneto-acoustic wave.

3.2. 22 June 2011 [Sunspot]

The second AIA observation is of active region AR11236 on 22 June 2011. The two arcs that outline the loop are shown in Figure 4(a). The loop has solar coordinates of (338,146) arcseconds at 15:13UT. Running-difference images for the area outlined by the two arcs in (a) are shown in (b)–(d) of Figure 4. This loop is rooted in a sunspot umbra, unlike the example analysed in Section 3.1, which is situated over a plage region.

We can see from Figure 4 that there are clear intensity bands indicating PDs in the three wavelengths. This could be an indication of their behaviour; for

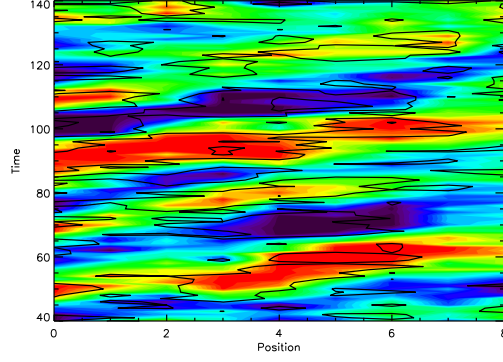


Figure 3. Contour plot of the 193 Å running-difference with 131 Å overplotted (thick black lines) for 22 September 2011.

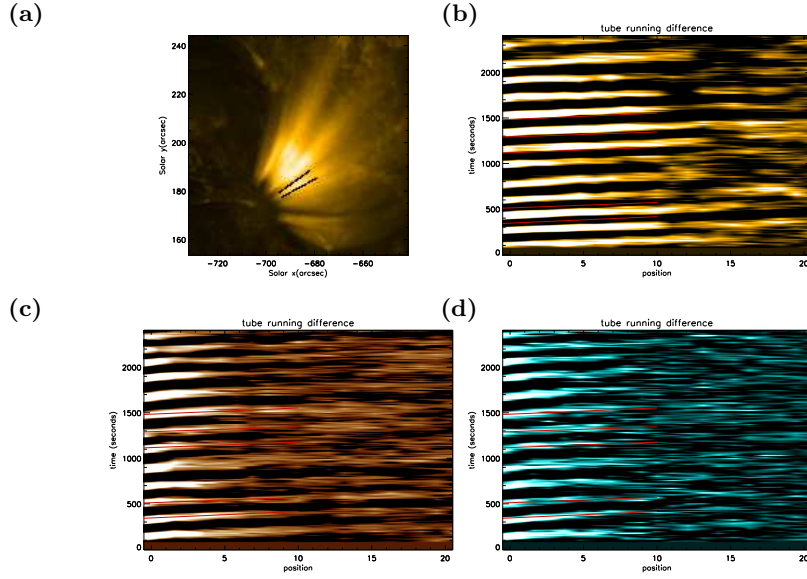


Figure 4. (a) 171 Å intensity image with the analysed loop outlined by the black lines. (b)–(d) Running difference images for the 171 Å, 193 Å, and 131 Å passbands, respectively for 22 June 2011. The red lines correspond to the gradient of the intensity bands from the 193 Å running-difference.

near-harmonic waves (over this relatively short time interval), we would expect the wave amplitude to be approximately constant, the bands to be equally bright, and very straight (as the wave-propagation speed does not depend on its amplitude in the linear regime). This is what we observe in Figure 4. For flows, one could envisage a more random behaviour with variations in the strength of the flows (*i.e.* the amplitude of the PDs) and hence the speed (*i.e.* the slope of the bands). This could be an explanation for the irregularity seen in the bands in Figure 1. Using the overplotted lines as an aid, the 131 Å bands

may have a slightly greater gradient than the 193 Å. The 171 Å bands seem to have approximately the same gradient but it is difficult to get an accurate measurement due to the fact the bands do not match spatially. The velocities are calculated in the same way as in the previous example and are displayed in Table 2. The straight, parallel nature of the bands in Figure 4(b) – (d) is reflected in the relatively small range of speeds between the different bands in Table 2. For an non-sunspot example, a much greater disparity between different bands was found (Table 1).

Table 2. Average velocities associated with running-difference for all wavelengths (in kms^{-1}) for 22 June 2011. The velocities in the brackets show the lower and higher estimates.

Band	131 Å	171 Å	193 Å
1	75(33–298)	88(44–288)	92(40–277)
2	62(29–557)	100(54–733)	111(42–177)
3	67(27–134)	111(54–812)	112(40–143)
4	95(38–191)	104(45–365)	123(45–163)
5	86(37–257)	88(43–335)	97(44–580)

From Table 2 we can see that the average velocities of the PDs generally increase from 131 Å to 193 Å. If we assume a characteristic temperatures of 0.4 MK for the 131 line, 0.8 MK for 171 Å and 1.2 MK for 193 Å, the sound speed increases by a factor of 1.187 from 131 Å to 171 Å and by 1.192 from 171 Å to 193 Å. The average velocities in the table match these factors reasonably well.

Figure 5 again shows cuts at positions 1, 3, 5, and 7 for the three different wavelengths. At position 1 the three wavelengths match quite well for most of the time. The 131 Å and 193 Å lines match very well throughout, but the 171 Å line seems to have a greater frequency than the 193 Å and 131 Å lines. It is only in phase for times greater than 1200 seconds. The 193 Å and 131 Å lines continue to match at positions 3 and 5, with the 171 Å line remaining out of phase with the others. At position 7 the 131 Å and 193 Å signals have now drifted slightly out of phase with one another and the 171 Å line has remained approximately half a wavelength out of phase.

Figure 6 shows a contour plot of the 193 Å running difference with the 131 Å contours overplotted. The bands in the 193 Å contour plot are outlined quite well by the 131 Å contours. There is evidence of the gradients of the bands increasing in the 131 Å contours. The gradient of the 131 Å contours may be slightly greater than the 193 Å contours but not by a large amount. The similarities between the 193 Å and 131 Å passbands at sunspot locations is discussed further in Section 5.

If we consider the velocities calculated from the running-difference images, there does seem to be a systematic dependence on the temperature, which fits with the slow magneto-acoustic wave interpretation. From Figure 5 it appears that the 171 Å PDs are travelling at a different velocity than the others, which only drift slightly out of phase as they travel further along the loop.

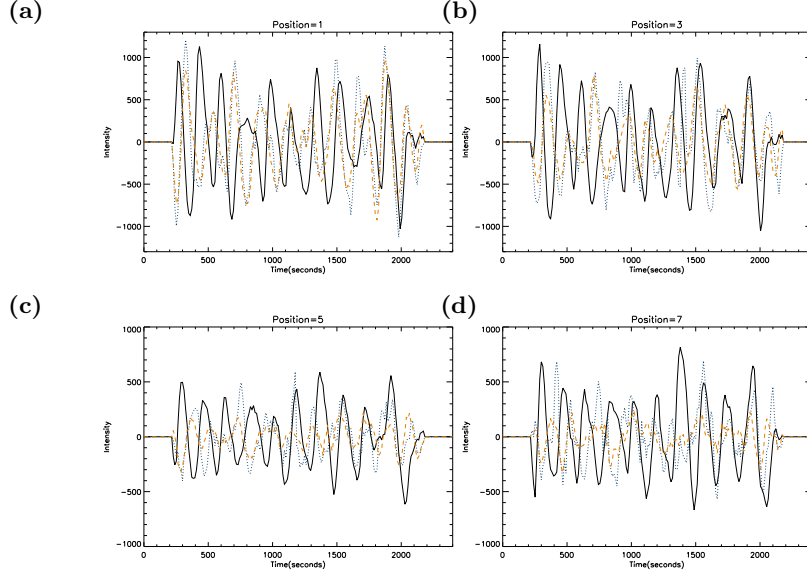


Figure 5. Cuts through de-trended intensities for 171 Å (black solid), 193 Å (orange dashed), and 131 Å (blue dotted) for different positions along the tube, for 22 June 2011.

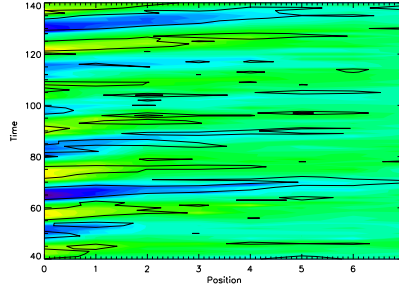


Figure 6. Contour plot of the 193 Å running-difference with 131 Å overplotted (thick black lines) for 22 June 2011

3.3. Alternative Methods for Calculating the Velocities

The velocities in Tables 1 and 2 are calculated from manually measuring the gradient of the PDs in the running-difference images (Figures 1 and 4). Although this method is known to give a reasonable estimate of the velocities, it is subjective (*i.e.* user dependent), and the errors associated with it can be substantial (Yuan and Nakariakov (2012)). This method will be referred to as method 1 (M1). We have used a further two methods to calculate the velocity. Method 2 (M2): for each intensity band we find the location of the maximum for each position of the band. The positions of the maximum are then plotted against position along the loop and the gradient of a line fitted to these points is taken to be an estimate of the velocity. Method 3 (M3): we find the correlation and

the time lag between the signals at each position. In this case, the lag gives an estimate of the velocity. This is the same method used by Tian *et al.* (2011) and McIntosh *et al.* (2012) to calculate the velocities. The errors associated with M2 and M3 range between $5\text{--}15\text{kms}^{-1}$. The velocities are calculated for both the sunspot (22 June 2011) and non-sunspot (22 September 2011) examples using M2 and M3 and are displayed in Tables 3 and 4.

Table 3. Calculated velocities using methods 2 and 3 (M2/M3) for PDs associated with running-difference images, for all wavelengths (in kms^{-1}), for 22 June 2011.

Band	131 Å	171 Å	193 Å
1	87/113	140/138	120/168
2	90/90	124/128	147/170
3	86/62	116/132	141/126
4	92/117	105/123	120/151
5	51/82	100/121	124/131

Table 4. Calculated velocities using method 2 and 3 (M2/M3) for PDs associated with running-difference images, for all wavelengths (in kms^{-1}), for 22 September 2011.

Band	131 Å	171 Å	193 Å
1	30/39	27/60	27/59
2	91/100	98/63	66/65
3	58/62	71/63	61/66
4	45/41	40/60	53/86
5	36/41	49/61	26/40

The velocities calculated using method 2 are similar to those found using M1, with the mean values across the five bands within $5\text{--}20\text{ kms}^{-1}$ of each other. Our earlier results concerning the temperature dependence are still present; for the sunspot example (22 June 2011) we still find a temperature dependence but no clear dependence is present in the non-sunspot example (22 September 2011) using M2. The velocities calculated using M3 are greater than the velocities calculated by M1 and M2 for both examples, but not by a significant amount. Even with this increase in the velocities we again confirm the results found using M1. We can be confident that the results found in Sections 3.1 and 3.2 are not dependent on the way that we have measured the gradient.

3.4. Other Examples

In total we have identified 41 loops over eight active regions. Information on the eight data sets we have considered is displayed in Table 5.

Table 5. The eight data sets that contain the 41 examples studied.

Data Set	Date	Start Time
A	16 September 2010	12:05 UT
B	19 March 2011	12:55 UT
C	22 September 2011	00:35 UT
D	3 April 2011	15:20 UT
E	1 October 2011	13:35 UT
F	28 March 2011	14:45 UT
G	24 August 2011	09:40 UT
H	22 June 2011	15:13 UT

The same analysis has been undertaken for the 39 other examples and characteristic velocities using the three methods and temperature dependence are displayed in Table 6. Speeds in brackets correspond to intensity bands that are less clear in the respective running-difference images. For the examples we have investigated here there are two categories of less clear: i) in some cases the PDs did not persist for the entire time interval (and hence we only had a limited number of bands to measure) or ii) the PDs only showed up near the footpoint of the loops (and hence the slope became difficult to measure). It is interesting to note these cases are always non-sunspot examples, again highlighting the more intermittent, varying nature of non-sunspot PDs. Each example has been categorised in one of two categories: the velocity of the PDs are dependent on temperature or they are independent of temperature. Two of the three methods need to show a temperature dependence for that example to be defined as temperature dependent. For the majority of cases the three methods are consistent and the examples that are not, are explained by the superscript. The solar co-ordinates given in the table correspond to the footpoints of the loop, in arcseconds. Whether or not the loop footpoints are located in a sunspot is also indicated in the S column in Table 6.

The characteristic speeds displayed in Table 6 are the mean of the average velocities calculated from the intensity bands. In 38 out of 41 of the examples, whether their velocities are dependent on temperature depends on whether they are located at sunspot or non-sunspot location, *i.e.* double Ys or Ns. PDs that are dependent on temperature are mainly found in sunspots and PDs whose velocity are not dependent on temperature are mainly found in non sunspot regions. In 11 of the 13 (85%) sunspot examples the PDs are dependent on the temperature, and at non-sunspot locations 27 out of the 28 (96%) examples the PDs are not dependent on temperature. Of these 27, eight examples showed a temperature dependence in one of the methods for calculating velocity. Hence, for

Table 6. The location, characteristic velocities for the three methods (M1/M2/M3) and temperature dependence (TD) of all the examples considered. Parentheses indicate that the intensity bands are less clear in the running-difference image. ¹ velocities calculated using M2 show a TD. ² velocities calculated using M1 show a TD. ³ velocities calculated using M1 does not show a TD. ⁴ velocities calculated using M3 show a TD.

Data Set	Loop Coords	131 Å	171 Å	193 Å	Temp Depen.	S
A	(-309,-377)	135/66/99	109/81/92	109/61/87	N	N
	(-289,-375)	(124/88/113)	98/90/98	121/120/127	N ¹	N
	(-288,-361)	(142/155/151)	146/86/124	142/81/97	N	N
	(-110,-499)	85/59/68	57/49/59	128/118/132	N	N
	(-94,-500)	(114/85/115)	125/165/157	119/108/122	N	N
	(-83,-501)	(70/57/64)	78/41/53	83/76/81	N ²	N
	(-69,-499)	(60/52/100)	53/49/70	82/94/105	N	N
	(-69,-442)	68/58/78	88/78/82	105/92/119	Y	Y
	(-67,-431)	53/53/79	67/92/108	72/104/125	Y	Y
B	(-73,-383)	(85/62/111)	91/74/61	85/60/75	N	N
	(-174,-416)	(66/65/117)	103/102/108	65/62/109	N	N
	(-72,-346)	(107/73/95)	62/76/81	80/75/111	N	N
C	(-670,204)	39/50/69	36/40/38	39/55/58	N	N
	(-672,189)	87/53/73	58/50/58	87/85/100	N	N
	(-673,154)	75/85/76	73/125/101	81/96/110	N	N
	(-662,133)	80/108/124	84/102/109	94/89/85	N ²	N
D	(289,329)	29/24/22	44/44/37	43/48/54	Y ³	Y
	(289,339)	38/43/42	49/46/60	57/81/75	Y	Y
	(282,341)	40/40/53	44/47/71	63/96/102	Y	Y
E	(496,95)	(96/77/77)	73/47/64	94/95/113	N	N
	(479,92)	(98/71/110)	105/61/77	108/91/104	N ²	N
	(459,90)	(96/83/88)	66/62/75	80/99/105	N	N
	(442,100)	(75/113/99)	102/60/88	127/87/97	N ²	N
	(397,159)	96/92/131	66/69/79	84/111/114	N	N
	(398,167)	125/111/87	126/85/89	115/75/120	N	N
	(436,147)	39/70/75	37/54/55	44/61/38	N	Y
F	(-208,-206)	(63/66/111)	65/98/90	78/67/112	N ²	N
	(-156,-157)	(118/90/106)	71/108/134	99/67/90	N	N
	(-203,-212)	95/57/75	57/92/110	77/153/120	Y ³	N
	(-424,-204)	(106/130/132)	107/129/126	111/154/128	N ²	N
G	(555,174)	68/80/64	71/93/117	77/101/127	Y	Y
	(557,180)	71/58/63	76/76/64	95/101/111	Y	Y
	(552,184)	94/78/93	111/90/99	116/113/119	Y	Y
H	(559,178)	97/64/81	124/106/125	129/96/121	N ²	N
	(538,154)	131/97/72	140/114/138	130/107/112	N	N
	(530,141)	135/83/117	142/126/133	123/84/109	N	N
	(461,263)	66/39/51	83/69/95	76/61/96	N ⁴	Y
	(463,260)	62/44/53	91/91/117	97/95/125	Y	Y
	(446,259)	71/77/75	86/103/100	93/114/129	Y	Y

the examples analysed here, the dependence of the PD velocity on temperature seems to correlate with the location (sunspot or non-sunspot region).

4. Properties of PDs Across an Active Region

These PDs are thought to arise from the leakage of global p -modes into the solar atmosphere (De Pontieu, Erdélyi, and De Moortel, 2005; De Moortel and Rosner, 2007; Malins and Erdélyi, 2007). This is known to lead to periods of approximately five minutes for non-sunspot locations and three minutes above sunspots. We will now investigate how properties such as period and velocity change across a smaller scale, *i.e.* how they change across a single set of sunspot and non-sunspot loops. Again we consider the two primary active regions analysed in Section 3 and focus on the 171 Å passband. Eight arcs are identified in this set of sunspot loops and we study over which scale the properties of the PDs change. Figure 7 shows the area in which the eight arcs are defined for the first example (22 June 2011). Arc 1 is located closest to the left side in Figure 7 and arc 8 is located closest to the right-hand side. Running differences are then calculated in the usual way.

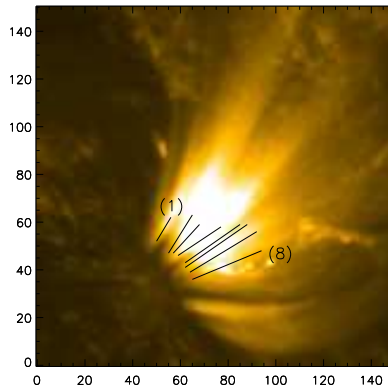


Figure 7. 171 Å intensity image showing where the eighth arcs are defined for AR11236 at 15:13UT on the 22 June 2011.

Figure 8 shows cuts through running-difference images for the eight arcs. Panels (a), (c), (e), and (g) are for arcs 1–4 and panels (b), (d), (f), and (h) are for arcs 5–8. The black solid lines represents arc 1 in (a), (c), (e), and (h) and arc 5 in (b), (d), (f), and (h). The green dotted lines represent arcs 2 and 6, the red dashed line arcs 3 and 7 and orange dot-dashed lines represents arcs 4 and 8.

It is clear from Figure 8 that arcs 5–8 are approximately in phase for all positions along the arc. Arcs 2–4 are also in phase for all positions but arc 1 is slightly out of phase with 2–4. To quantify these phase differences, we calculate the cross correlation between each loop at all positions as a function of the lag.

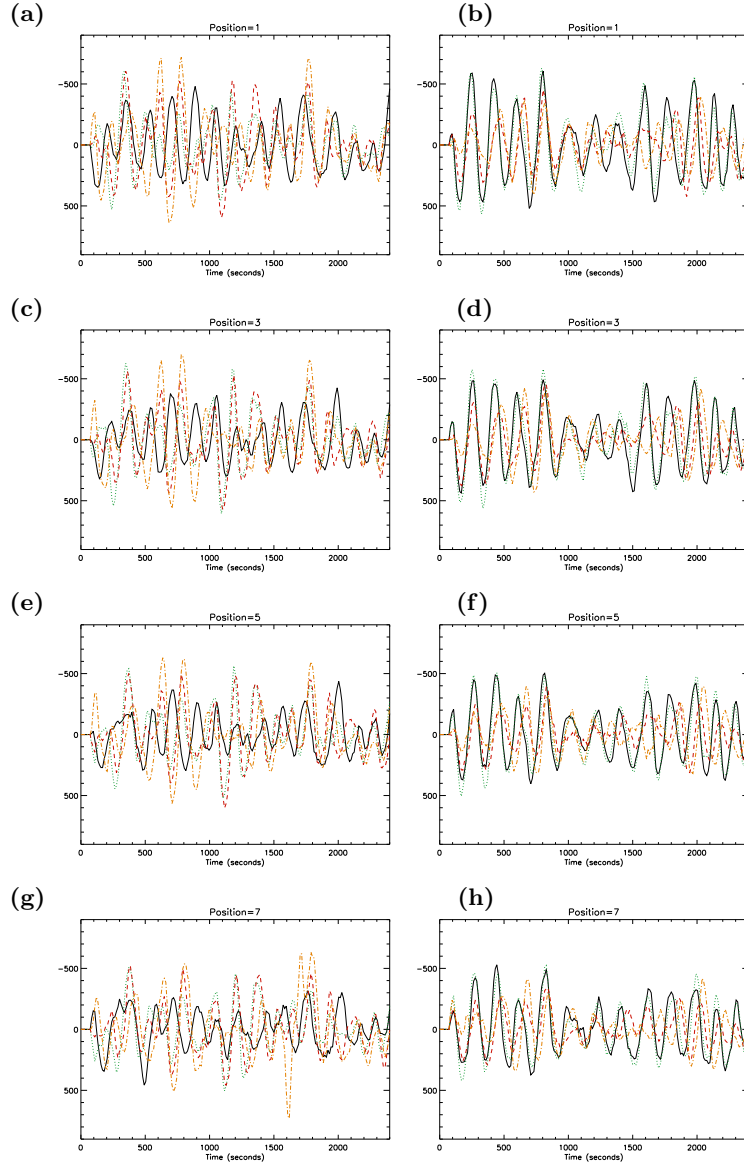


Figure 8. Cuts through the 171 Å running-difference images for arcs 1–8 at all positions for 22 June 2011. (a), (c), (e), and (g) show arcs 1–4 and (b), (d), (f), and (h) show arcs 5–8. The solid black lines corresponds to arcs 1 and 5, the green dotted lines to arcs 2 and 6, red dashed to 3 and 7, and orange dot-dashed to 4 and 8.

Table 7 shows the maximum correlation between two loops and the time lag at which this correlation is achieved.

This analysis is repeated for positions 3, 5, and 7 and the corresponding correlation tables are in the appendix. From Table 7 we can see that arcs 2–4

Table 7. Cross correlation between 171 arcs at position 1 along the loop defined on the 22 June 2011. The subscript denotes the lag (i units of 12 seconds) where the maximum correlation is found. The table is symmetric, and the blank spaces would have the same values as their corresponding location, with the sign of the lag changing.

Arc	1	2	3	4	5	6	7	8
1	1	0.365 ₋₃	0.187 ₋₂	0.471 ₅	0.344 ₋₁₀	0.381 ₋₁₀	0.360 ₈	0.477 ₉
2		1	0.815 ₁	0.215 ₂	0.273 ₅	0.256 ₅	0.264 ₋₈	0.181 ₁₂
3			1	0.476 ₁	0.384 ₃	0.356 ₃	0.263 ₋₉	0.130 ₋₁₄
4				1	0.569 ₁	0.522 ₁	0.582 ₃	0.451 ₄
5					1	0.897 ₀	0.582 ₂	0.297 ₄
6						1	0.721 ₂	0.373 ₃
7							1	0.687 ₁
8								1

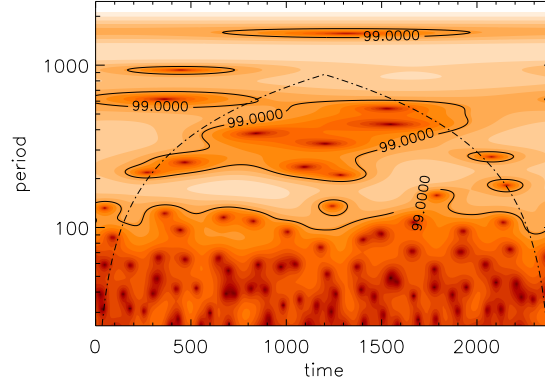


Figure 9. Wavelet analysis for arc 1 on 22 June 2011 at position 1.

have maximum correlation with each other at relatively small lag positions, i.e. loops 2–4 are mostly in phase with each other. Arcs 5–8 are also approximately in phase at this position. The lag where the maximum correlation occurs becomes greater when you consider two arcs that are not located next to each other. The fact that the PDs do not correlate over the entire extent of this ensemble of sunspot loops suggests the underlying driver changes on smaller scales. However, we have to keep in mind that some of the lag could also be caused by the fact that the starting points of the arcs do not line up perfectly.

The periods of these disturbances are calculated using a wavelet transform (Torrence and Compo 1998) with the Morlet function as the mother wavelet and are displayed in Table 8. The range of periods is calculated using the bottom and top of the band that is above the confidence interval. An example wavelet is shown from arc 1 position 1 in Figure 9.

From Table 8 we can see that the PDs associated with all arcs have approximately the same period which appears centred around 180 seconds (three

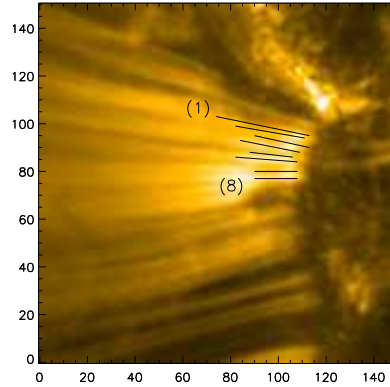
Table 8. Table showing the periods and characteristic 171 Å velocity for arcs 1–8 for 22 June 2011.

Arc	Period[s]	Char. Velocity[kms ⁻¹]
1	150–200	131
2	100–200	128
3	120–190	130
4	150–210	135
5	160–200	152
6	160–200	136
7	150–210	167
8	150–200	143

minutes) as expected for sunspot loops (De Moortel, Ireland, and Walsh, 2000). The velocities of the PDs as seen in the 171 Å passband are also displayed. Arcs 1–4 all propagate with approximately the same speed. Arcs 5–8 also propagate with approximately the same speed as each other but at a slightly greater speed than arcs 1–4.

4.1. 22 September 2011 (Non Sunspot)

This analysis is also done on the other primary data set (22 September 2011). We define eight arcs (Figure 4.1) between the two lines displayed in Figure 4.1, with arc 1 again closest to the top of the image and arc 8 defined closest to the bottom. Running differences are constructed in the usual way and cuts are taken at several positions and are displayed in Figure 11.

**Figure 10.** 171 Å intensity image showing where eight arcs are defined for AR11301 at 00:35UT on 22 September 2011.

Each line in Figure 11 is defined in the same way as Figure 8. We can see that arcs 6–8 (green dotted/red dashed/orange dot-dashed in the right-hand

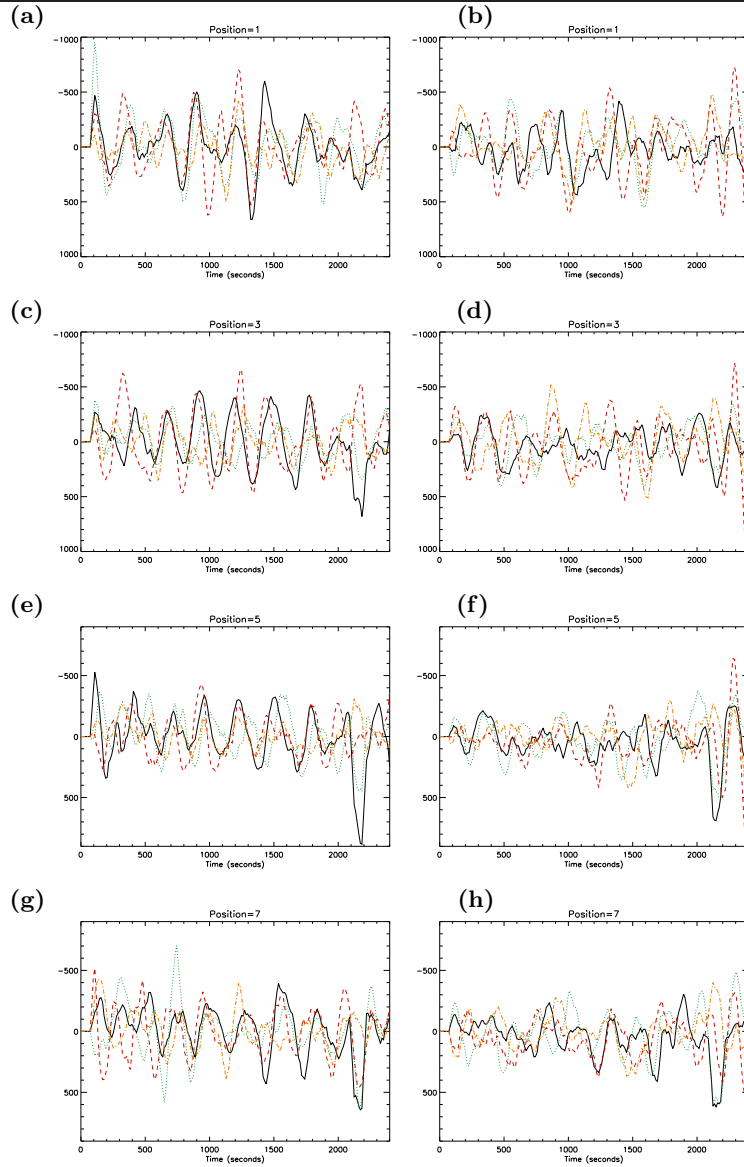


Figure 11. Cuts through the 171 Å running-difference images for arcs 1–8 at all positions for 22 September 2011. (a), (c), (e), and (g) show arcs 1–4 and (b), (d), (f), and (h) show arcs 5–8. The solid black lines correspond to arcs 1 and 5, the green dotted line to arcs 2 and 6, red dashed to 3 and 7, and orange dot-dashed to 4 and 8.

column of graphs) match very well for all positions. Arc 5 appears to match well at some times but is completely out of phase at others. Arcs 1, 2, and 4 are almost in phase at position 1, whilst the red dashed line (arc 3) is out of phase at certain times. At positions 3 and 5, the arc 2 line (green dotted line in left

hand column) is approximately in phase with the others and at position 7 there is some evidence of them starting to become out of phase. We have calculated the cross correlation for this example and the results are displayed in Table 9.

Table 9. Cross correlation between 171 Å arcs at position 1 along the loop for 22 September 2011. The subscript denotes the lag (in units of 12 seconds) where the maximum correlation is found.

Arc	1	2	3	4	5	6	7	8
1	1	0.659 ₁	0.506 ₀	0.409 ₋₂₉	0.095 ₀	0.252 ₋₆	0.274 ₋₉	0.170 ₋₆
2		1	0.406 ₋₁	0.406 ₁	0.081 ₁₁	0.393 ₋₇	0.173 ₋₉	0.098 ₂₇
3			1	0.244 ₉	0.106 ₁₁	0.161 ₋₇	0.229 ₋₃	0.229 ₋₁
4				1	0.156 ₁₄	0.398 ₋₉	0.316 ₋₁₁	0.476 ₋₈
5					1	0.144 ₁	0.226 ₁₂	0.340 ₋₅
6						1	0.403 ₋₂	0.267 ₀
7							1	0.389 ₁
8								1

There is no clear pattern in Table 9. On average, arcs correlate better with arcs located close to them. There are exceptions though. For example, arc 4 only has a high correlation with arc 2, arcs 6–8 on average are well correlated with most maximum correlations occurring within one or two time frames. However, the correlation values are overall lower than in the previous case, which could be due to the arc footpoints not lining up very well. The lags associated with arcs 1 and 4 and arcs 2 and 8 are large but these do not give a true reflection of the correlation between the two arcs as a lag in this range corresponds to approximately a full period. These arcs are actually in phase as seen in Figure 11. The dominant periods and characteristic velocities for this example are displayed in Table 10.

Table 10. Table showing the periods and characteristic 171 Å velocity for arcs 1–8 for 22 September 2011.

Arc	Period(s)	Char. Velocity(kms ⁻¹)
1	250–300	74
2	270–320	76
3	270–320	61
4	260–310	93
5	200–290	88
6	300–360	84
7	270–300	109
8	270–320	91

As in the previous example the dominant periods are approximately constant for each of the arcs. As we would expect given this example is not a sunspot

region, the dominant periods are longer and closer to five minutes (300 seconds). The velocities for this example seem to increase slightly as we move down the arcs.

The periods of the PDs are constant across the two active regions in both cases. The velocities stay approximately constant with some variation, where the small variations could possibly be due to changes in the inclination angles.

5. Removing the Cool Emission from the 193 Å Passband

As shown by Del Zanna *et al.* (2011) using simultaneous *Hinode*/EIS spectra and SDO/AIA images, AR loop legs produce strong Fe VIII and Fe IX “cool” emission dominating the 131 and 171 Å bands. The 193 Å band is multithermal, in that strong emission from Fe VIII and Fe IX lines alongside Fe XI and Fe XII is observed. Weak emission from a range of even lower temperature lines (mostly from O V and Fe VII) is also present. As described by Del Zanna *et al.* (2011), the atomic data for Fe IX, Fe XI, and Fe XII are relatively well understood, while the Fe VIII data are more uncertain. The Fe VII data are very uncertain and have not yet been included in the CHIANTI database (Landi *et al.*, 2012).

We have devised a rough method to estimate the main cool contribution (from Fe VIII and Fe IX) to the 193 Å passband, in order to subtract it, and study the properties of the hot ($T > 1$ MK) emission in the band. The loop legs we have chosen have strong emission in the 131 Å and 171 Å passband, formed in the $\log T[K] = 5.5 - 5.9$ range. There is observational evidence based on spectroscopy that at each location the plasma distribution in loop legs is nearly isothermal (*e.g.* De Zanna and Mason (2003), De Zanna, O’Dwyer, and Mason (2011), Tripathi *et al.* (2009)). As a first approximation, it is therefore reasonable to assume that at each location the plasma is isothermal. With this assumption, we then estimate the isothermal temperature and emission measure of the main cool component for each pixel using the observed 171 Å and 131 Å count rates and the respective response functions calculated using CHIANTI v.7 (Landi *et al.*, 2012) (The 193 response function has been calculated using the method outlined in De Zanna, O’Dwyer, and Mason (2011)). We simply divide the observed counts by the responses and take the intersection of the curves (see Figure 12) as the estimate of the isothermal temperature.

The method is basically the Emission Measure Loci one (De Zanna and Mason (2003)) applied to the AIA bands. We define the value where the dot-dashed line in the left plot in Figure 12 cross the x -axis as the isothermal temperature $[T_i]$. The value of the emission measure at the isothermal temperature (the value where the dot-dashed line in the left plot crosses the y -axis) as $E(T_i)$ and the value of the 193 Å response function at the isothermal temperature (the value where the dot-dashed line in the right plot crosses the y -axis) as $R(T_i)$. We can now estimate the contribution (in DN s^{-1}) to the 193 Å band due to the Fe VIII and Fe IX lines $[C]$ by $C = E(T_i)R(T_i)$. for a given pixel. This gives us an estimate of the main cool contribution for a given pixel to the 193 Å emission. This is a lower estimate, given that it does not take into account lower temperature emission. De Zanna, O’Dwyer, and Mason (2011) measured the cool

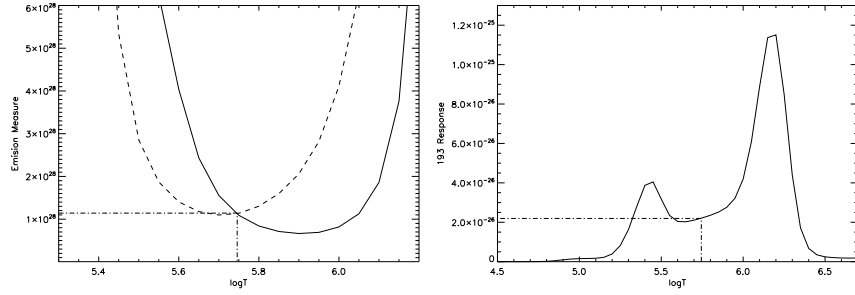


Figure 12. Left: Emission measure loci curves for a pixel in 171 Å (solid line) and 131 Å (dashed line). The dot-dashed line from the x -axis indicates the value of the isothermal temperature. The dot-dashed line that crosses the y -axis indicates the value of the emission measure at the isothermal temperature. The pixel is located at the loop footpoint and is from the sunspot example (22 June 2011). Right: the temperature response function for the 193 Å passband. The dot-dashed line from the x -axis indicates the value of the isothermal temperature. The dot dashed line that crosses the y -axis indicates the value of the response function at the isothermal temperature

emission in the 193 Å band in loop legs and footpoints to be as large as 40%. The present estimates provide a range of somewhat lower (but still significant) values, from about 10 to 40%. Once the cool emission is subtracted, we expect the dominant emission in the 193 Å band to be originating from Fe XI and Fe XII lines, i.e. from 1–2 MK plasma. We refer to this as the “hot” emission in the 193 Å band. The procedure was automated for all pixels in all 193 Å images and the cool contribution subtracted.

5.1. 22 June 2011 (Sunspot)

We have applied this technique to the two primary data sets analysed in Sections 3 and 4 to investigate how the properties of the PDs change in the 193 Å passband. We first plot the ratio of the cool contribution to the full emission for both examples (Figure 13).

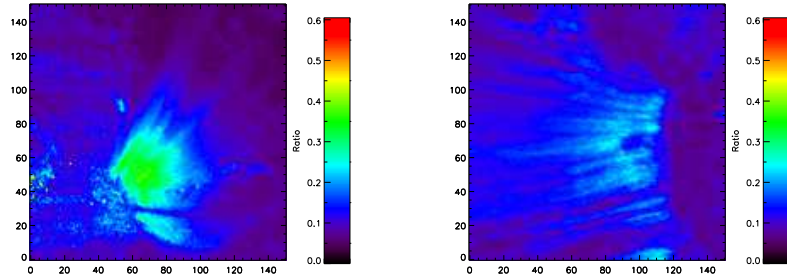


Figure 13. The ratio of the calculated cool emission to the full 193 Å emission for (left) the sunspot region (22 June 2011) and (right) the non-sunspot region (22 September 2011).

We can see from Figure 13 that there is a greater percentage of the cool emission at the sunspot example than the non-sunspot one. At the sunspot

example the cool contribution accounts for about 30–40% of the full emission, compared to 15 - 25% in the non-sunspot example.

The isothermal temperature is plotted in a similar way (Figure 14).

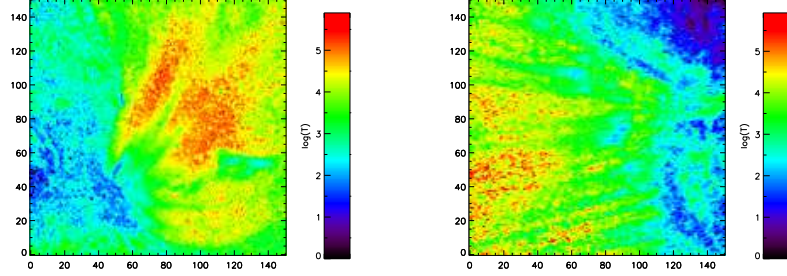


Figure 14. The calculated isothermal temperature for the sunspot region (22 June 2011) and (right) the non-sunspot region (22 September 2011).

From Figure 14 it is clear that there is a general increase in the (isothermal) temperature along the loops. This trend is observed in both the sunspot and non-sunspot examples.

We now compare the properties of PDs in the hot emission to those in the full emission. Figure 15 shows running-difference images created using the same data set as Figure 4, associated with the full emission (left) and the hot component only (right).

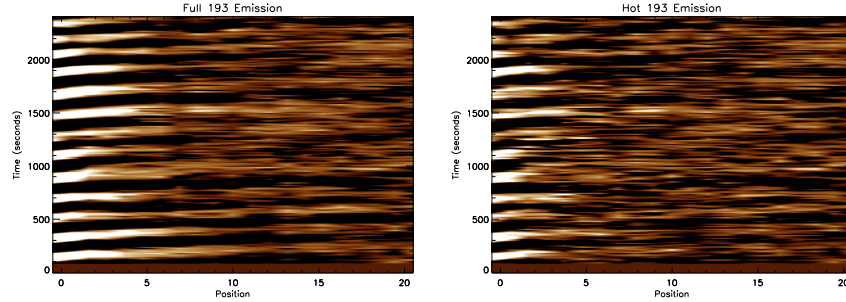


Figure 15. Running-difference images for the loop outlined in Figure 4. The left shows the running-difference associated with the full 193 Å emission. The right hand plot shows the running-difference associated with the hot 193 Å component only.

We can see from Figure 15 that there are clear differences in the PDs. PDs associated with the hot emission only propagate to positions 5–7 before they are no longer distinguishable compared to positions 12–14 in the full emission case. We calculated the velocities of the PDs in the cool, full, and hot data sets using the same methods as Section 3.3 and they are displayed in Table 11.

The velocities displayed in Table 11 show that on average the velocities of the PDs increase from the cool emission to the hot emission and this is consistent between the three methods for calculating the velocities.

Table 11. Characteristic velocities associated with running-difference images for the full, hot, and cool 193 Å emission for 22 June 2011, calculated using methods 1, 2, and 3.

Method	Cool	Full	Hot
1	69	98	118
2	70	89	104
3	98	123	143

5.2. 22 September 2011 (Non sunspot)

We now carry out the same analysis on our second primary data set (22 September 2011). The cool contribution to the 193 Å passband has been calculated in the same way as for the previous example. Running-difference images for this example are shown in Figure 16.

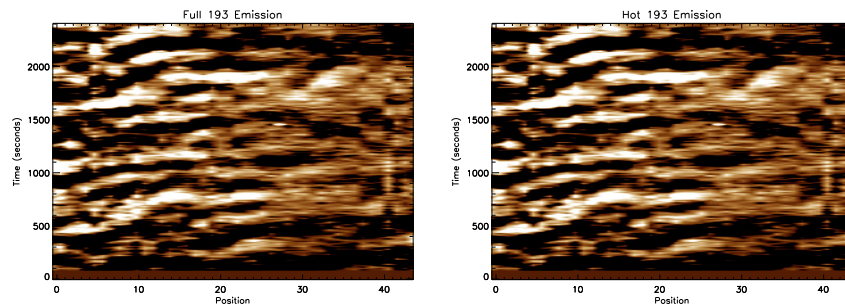


Figure 16. Running difference images for the loop outlined in Figure 1. The left shows the running-difference image associated with the full 193 emission. The right hand plot shows the running-difference image associated with the hot 193 contribution only.

For this example it is clear that the PDs associated with the hot emission have almost identical properties as the PDs from the full emission. They are exactly in phase, propagate the same distance along the loop, and have the same period.

In total we have carried out this analysis for seven loops. Four of these loops are located at sunspots and three at non-sunspot locations. PDs located at non-sunspot locations appear to be identical in the hot component and in the full emission. Also, the PDs seen in the cool emission are more similar to those seen in the 171 Å than the 131 Å passband. This is the case for all the non-sunspot examples studied. PDs seen in the hot emission and located at sunspots are not identical to the full emission PDs; they propagate a shorter distance along the loop before they become unidentifiable and travel at a slightly greater velocity. PDs associated with the cool contribution at these locations are very similar to those seen in the 131 Å passband.

This suggests that the PDs at sunspots are more likely to be slow magneto-acoustic waves. Indeed, when we have removed the cool contribution from the 193 Å line, the PDs have a slightly greater velocity than they have in the full emission case. Slow magneto-acoustic waves are expected to travel at the local sound speed and hence their velocity should increase with temperature. The main damping mechanism of slow magneto-acoustic waves is thought to be thermal conduction (De Moortel and Hood, 2004), which is consistent with the fact that the PDs in the hot emission case appear to damp quicker than in cooler lines. At non-sunspot locations the PDs associated with the hot emission are identical to those in the full emission. Along with the lower-intensity bands seen in the cool emission we can conclude that removing the cool contribution at non-sunspot regions has little to no effect on the properties of the PDs.

6. Discussions and Conclusions

The aim of this paper was to undertake a detailed investigation of the propagation speed of observed PDs to gain a greater insight into the temperature dependence of the PD properties.

In Section 3 we considered the velocities of PDs across the 131, 171, and 193 Å passbands. We studied two main examples, one located at a sunspot (22 June 2011) and one above a non-sunspot (plage) region (22 September 2011). The velocities calculated for the sunspot example displayed a temperature dependence, where velocities increased when the PDs were propagating in hotter plasmas. This velocity difference was found to be consistent with an interpretation in terms of slow magneto-acoustic waves, especially when the effect of removing the cooler contribution from the 193 Å emission is taken into account. The velocities found in the non-sunspot example did not display a clear temperature dependence. The velocities found were approximately constant across the three wavelengths. These results were confirmed by recalculating the velocities from a further two methods. This analysis was then used on a further 39 examples. Our total sample of 41 cases included 13 sunspot and 28 non-sunspot locations. The results suggest a strong relationship between whether or not the PDs are temperature dependent and whether the defined loops are located at a sunspot. Of the 13 loops located at sunspots, 11 showed PD propagation speeds that are temperature dependent, and for the 28 not located at sunspots, 27 did not show a temperature dependence. This suggests that PDs found at sunspots are far more likely to be temperature dependent and hence fit the slow-wave interpretation. For non-sunspot loops, the results are less clear. PDs located at these regions are less likely to be temperature dependent. This fact makes the slow magneto-acoustic wave interpretation less likely, as a slow wave would adjust its velocity to the local sound speed.

In Section 4 we studied how the properties of these PDs change across a set of active region loops and a set of sunspot loops. It was found that the velocities of the PDs can change across an active region but the periods stay constant across the active region. This trend was found for both the sunspot and non-sunspot examples.

In the final section we considered the effect of removing the cool contribution in the 193 Å passband on the properties of the PDs. A rough method was devised to remove the contribution due to the cooler ions and this technique was used on seven examples. We found that the properties of the PDs do not change when the cool contribution is removed when considering loops at non-sunspot locations. Properties of PDs associated with loops located at sunspots did change when the cool contribution is removed. The PDs seen in the hot emission damp more rapidly than the PDs seen in the full emission cases. The velocities of the PDs in the hot emission are found to be slightly greater than those in the full emission. This analysis further suggests that PDs seen at sunspots agree with the wave interpretation, as this interpretation explains the increase of the PDs velocity and the rapid damping (as thermal conduction is more efficient at higher temperatures). Removing the cool contribution had little or no effect on the PDs at non-sunspot areas. Plasma is hotter at non-sunspot regions, and it is not surprising that there is less of an effect due to the cool emission at these regions.

Acknowledgements GK acknowledges the financial support of the STFC. IDM acknowledges support of a Royal Society University Research Fellowship. The authors would like to thank H. Tian for useful comments on the article.

Appendix

Correlation results for positions 3, 5, and 7 for the 22 June 2011 are displayed in Tables 12, 13, and 14.

Table 12. Cross correlation between 171 arcs at position 3 along the loop defined on the 22 June 2011. The subscript denotes the lag where the maximum correlation is found.

Arc	1	2	3	4	5	6	7	8
1	1	0.302 ₋₃	0.209 ₁₀	0.415 ₆	0.284 ₃	0.242 ₋₁₀	0.205 ₋₁₀	0.404 ₁₀
2		1	0.831 ₁	0.350 ₂	0.324 ₅	0.307 ₆	0.321 ₋₉	0.141 ₋₁₁
3			1	0.511 ₁	0.429 ₃	0.378 ₄	0.343 ₆	0.159 ₈
4				1	0.600 ₀	0.536 ₋₁₅	0.554 ₃	0.535 ₄
5					1	0.891 ₀	0.661 ₂	0.478 ₄
6						1	0.746 ₁	0.471 ₃
7							1	0.683 ₁
8								1

Correlation results for positions 3, 5, and 7 for the 22 September 2011 are displayed in Tables 15, 16, and 17.

Table 13. Cross correlation between 171 Å arcs at position 5 along the loop defined on the 22 June 2011. The subscript denotes the lag where the maximum correlation is found.

Arc	1	2	3	4	5	6	7	8
1	1	0.190 ₉	0.165 ₉	0.374 ₇	0.209 ₋₁₀	0.207 ₋₁₀	0.171 ₁₀	0.394 ₁₀
2		1	0.832 ₁	0.444 ₂	0.369 ₃	0.364 ₄	0.339 ₆	0.118 ₋₉
3			1	0.566 ₁	0.481 ₃	0.448 ₃	0.411 ₆	0.156 ₉
4				1	0.631 ₀	0.525 ₋₁₅	0.535 ₃	0.433 ₄
5					1	0.913 ₀	0.673 ₂	0.435 ₅
6						1	0.717 ₂	0.346 ₄
7							1	0.575 ₁
8								1

Table 14. Cross correlation between 171 Å arcs at position 7 along the loop defined on the 22 June 2011. The subscript denotes the lag where the maximum correlation is found.

Arc	1	2	3	4	5	6	7	8
1	1	0.154 ₋₂	0.114 ₁₀	0.143 ₆	0.192 ₃	0.152 ₋₁₁	0.164 ₋₁₀	0.288 ₁₀
2		1	0.849 ₁	0.445 ₃	0.412 ₄	0.390 ₄	0.363 ₆	0.157 ₁₀
3			1	0.554 ₂	0.521 ₃	0.492 ₃	0.394 ₆	0.186 ₆
4				1	0.488 ₀	0.416 ₁	0.444 ₃	0.369 ₄
5					1	0.889 ₀	0.662 ₂	0.481 ₅
6						1	0.719 ₂	0.466 ₄
7							1	0.547 ₁
8								1

Table 15. Cross correlation between 171 Å arcs at position 3 along the loop defined on the 22 September 2011. The subscript denotes the lag where the maximum correlation is found.

Arc	1	2	3	4	5	6	7	8
1	1	0.467 ₄	0.276 ₋₂	0.406 ₋₁₅	0.389 ₋₂	0.311 ₋₃	0.114 ₋₉	0.316 ₋₄
2		1	0.378 ₋₆	0.330 ₀	0.480 ₋₄	0.500 ₋₈	0.132 ₋₁₀	0.365 ₁₄
3			1	0.290 ₋₁₅	0.248 ₅	0.199 ₋₁	0.209 ₉	0.198 ₋₃
4				1	0.243 ₋₂	0.405 ₋₉	0.226 ₇	0.222 ₉
5					1	0.351 ₋₂	0.111 ₀	0.267 ₁₄
6						1	0.320 ₁	0.204 ₋₁₁
7							1	0.403 ₀
8								1

Table 16. Cross correlation between 171 Å arcs at position 5 along the loop defined on the 22 September 2011. The subscript denotes the lag where the maximum correlation is found.

Arc	1	2	3	4	5	6	7	8
1	1	0.476 ₂	0.451 ₋₂	0.194 ₄	0.524 ₀	0.521 ₀	0.196 ₂	0.074 ₆
2		1	0.484 ₋₆	0.169 ₋₃	0.445 ₀	0.177 ₋₂	0.273 ₃	0.127 ₄
3			1	0.218 ₄	0.157 ₄	0.266 ₃	0.211 ₇	0.083 ₋₁₅
4				1	0.163 ₁₄	0.194 ₋₁₄	0.248 ₁₂	0.217 ₁₂
5					1	0.428 ₀	0.356 ₂	0.210 ₋₁₄
6						1	0.310 ₁	0.230 ₋₁₅
7							1	0.428 ₀
8								1

Table 17. Cross correlation between 171 Å arcs at position 7 along the loop defined on the 22 September 2011. The subscript denotes the lag where the maximum correlation is found.

Arc	1	2	3	4	5	6	7	8
1	1	0.508 ₀	0.499 ₋₃	0.130 ₁	0.474 ₀	0.353 ₀	0.244 ₋₁₃	0.212 ₈
2		1	0.347 ₋₂	0.371 ₋₁₅	0.221 ₂	0.346 ₂	0.239 ₂	0.177 ₁₄
3			1	0.224 ₅	0.187 ₀	0.400 ₀	0.122 ₂	0.073 ₋₁₁
4				1	0.209 ₁₀	0.194 ₋₁	0.066 ₁₁	0.278 ₋₁₀
5					1	0.489 ₋₁	0.313 ₋₁₃	0.182 ₋₁₅
6						1	0.171 ₋₁₅	0.262 ₋₁₄
7							1	0.275 ₁
8								1

References

- Banerjee, D, Teriaca, L, Gupta, G.R, Imada, S, Stenborg, G, Solanki, S.K: 2009 *Astron. Astrophys.* **499**, L29
- Banerjee, D, Gupta, G.R, Teriaca, L : 2011 *Space Sci. Rev.* **158**, 267.
- Berghams, D, Clette, F: 1999 *Solar Phys.* **186**, 207 ADS: 1999SoPh..186..207B, DOI: 10.1023/A:1005189508371.
- Berghams, D, McKenzie, D, Clette, F: 2001 *Astron. Astrophys.* **369**, 291
- Brooks, D.H, Warren, H. P : 2011 *Astrophys. J. Lett.* **501**, L217.
- Bryans, P, Young, P.R. Doschek, G.A:2010 *Astrophys. J.* **705**, 1012.
- Deforest, C.E, Gurman, J.B : 1998 *Astrophys. J. Lett.* **501**, L217.
- De Moortel, I, Ireland, J, Walsh, R.W: 2000 *Astron. Astrophys.* **355**, L23.
- De Moortel, I, Hood, A.W: 2003 *Astron. Astrophys.* **408**, 755.
- De Moortel, I, Hood, A.W: 2004 *Astron. Astrophys.* **415**, 705.
- De Moortel, I, Hood, A.W, Gerrard, C.L, Brooks, S.J: 2004 *Astron. Astrophys.* **425**, 741
- De Moortel, I: 2009 *Space Sci. Rev.* **149**, 65.
- De Moortel, I, Rosner, R: 2007 *Solar Phys.* **246**, 53 ADS: 2007SoPh..246...53M, DOI: 10.1007/s11207-007-0392-6.
- De Pontieu, B, Erdélyi, R, De Moortel, I : 2005 *Astrophys. J. Lett.* **624**, L61.
- De Pontieu, B, McIntosh, S.W: 2010 *Astrophys. J.* **722**, 1013.

- De Pontieu, B, McIntosh, S.W, Carlsson, M, Hansteen, V.H, Tarbell, T.D, Boerner, P: 2011 *Science* **331**, 55.
- De Pontieu, B, McIntosh, S.W, Hansteen, V.H, Schrijver, C.J: 2009 *Astrophys. J. Lett.* **701**, L1.
- Del Zanna, G: 2008 *Astron. Astrophys.* **481**, L49.
- Del Zanna, G, Mason, H.E: 2003 *Astron. Astrophys.* **406**, 1089.
- Del Zanna, G, O'Dwyer, B, Mason, H.E: 2011 *Astron. Astrophys.* **535**, A46.
- Dere, K.P, Landi, E, Young, P.R, Del Zanna, G. and Landini, M, Mason, H.E : 2009 *Astron. Astrophys.* **498**, 915.
- Doschek, G.A, Mariska, J.T, Warren, H.P, Brown, C.M, Culhane, J.L, Hara, H *et al.*: 2007 *Astrophys. J. Lett.* **607**, L109.
- Hara, H: 2008 *Astronomical Herald* **101**, 497.
- Hara, H, Watanabe, T, Harra, L.K, Culhane, J.L, Young, P.R, Mariska, J.T, Doschek, G.A.: 2008 *Astrophys. J. Lett.* **678**, L67.
- Harra, L.K, Sakao, T, Mandrini, C.H, Hara, H, Imada, S, Young, P.R, van Driel-Gesztelyi, L, Baker, D.: 2008 *Astrophys. J. Lett.* **677**, L159.
- He, J.S, Marsch, E, Tu, C.Y, Guo, L.J, Tian, H: 2010 *Astron. Astrophys.* **516**, A14.
- Kamio, S, Peter, H, Curdt, W, Solanki, S.K: 2011 *Astron. Astrophys.* **532**, 96.
- Kitagawa, N, Yokoyama, T, Imada, S, Hara, H: 2010 *Astrophys. J.* **721**, 744.
- Krishna Prasad, S, Banerjee, D, Gupta, G.R: 2011 *Astron. Astrophys.* **528**, L4.
- Landi, E, Del Zanna, G, Young, P.R, Dere, K.P, Mason, H.E: 2012 *Astrophys. J.* **744**, 99.
- Malins, C, Erdélyi, R: 2007 *Solar Phys.* **246**, 41 ADS: 2007SoPh..246...41M, DOI: 10.1007/s11207-007-9073-8.
- Mariska, J.T, Muglach, K: 2009 *Astrophys. J.* **713**, 573.
- Marsch, E, Tian, H, Sun, J, Curdt, W. and Wiegmann, T: 2008 *Astrophys. J.* **685**, 1262.
- Marsh, M.S, I, Walsh, R.W: 2009 *Astrophys. J. Lett.* **706**, L76.
- Marsh, M.S, I, Walsh, R.W, Plunkett, S: 2009 *Astrophys. J.* **697**, 1674
- McEwan, M.P, De Moortel, I: 2006 *Astron. Astrophys.* **448**, 763.
- McIntosh, S.W, De Pontieu, B: 2009 *Astrophys. J. Lett.* **706**, L80.
- McIntosh, S.W, Innes, D.E, De Pontieu, B, Leamon, R.J.: 2010 *Astron. Astrophys.* **510**, L2.
- McIntosh, S.W, Tian, H, Sechler, M, De Pontieu, B: 2012 *Astrophys. J.* **749**, 60.
- Murray, M.J, Baker, D, van Driel-Gesztelyi, L, Sun, J: 2010 *Solar Phys.* **261**, 253. ADS: 2010SoPh..261..253M, DOI: 10.1007/s11207-009-9484-9.
- Nakariakov, V.M, Verwichte, E, Berghams, D, Robbrecht, E : 2000 *Astron. Astrophys.* **362**, 1151.
- Nightingale, R.W, Aschwanden, M.J, Hurbert, N.E: 1999 *Solar Phys.* **190**, 249 ADS: 1999SoPh..190..249N, DOI: 10.1023/A:1005211618498.
- Nishizuka, N, Hara, H : 2011 *Astrophys. J. Lett.* **737**, L43.
- O'Dwyer, B, Del Zanna, G, Mason, H.E, Weber, M.A, Tripathi, D : 2010 *Astron. Astrophys.* **521**, A21
- Ofman, L, M.Romoli, Davila, J.M, Poletto, G, Kohl, J, Noci, G: 1997 A. Wilson (eds.) *Fifth SOHO Workshop: The Corona and Solar Wind Near Minimum Activity, University of Oslo* **404**, 571.
- Peter, H : 2010 *Astron. Astrophys.* **521**, A51
- Sakao, T, Kano, R, Narukage, N, Kotoku, J, Bando, T, De Luca, E.E : 2007 *Science* **318**, 1585.
- Schrijver, C.J, Title, A.M, Berger, T.E, Fletcher, L, Hurlbert, N.E, Nightingale: 1999 *Solar Phys* **187**, 261. ADS: 1999SoPh..187..261S, DOI: 10.1023/A:1005194519642.
- Tian, H, McIntosh, S.W, De Pontieu, B: 2011 *Astrophys. J. Lett.* **727**, L37.
- Tian, H, McIntosh, S.W, De Pontieu, B, Martínez-Sykora, J, Sechler, M, Wang, X: 2011 *Astrophys. J.* **738**, 18.
- Tian, H, McIntosh, S.W, Rifal Habbal, S, He, J: 2011 *Astrophys. J.* **736**, 130.
- Tripathi, D, Mason, H.E, Dwivedi, B.N, Del Zanna, G, Young, P.R. : 2009 *Astrophys. J.* **694**, 1256.
- Tsiklauri, D, Nakariakov, V.M: 2001 *Astron. Astrophys.* **379**, 1106.
- Roupe van der Voort, L, Leenaarts, J, De Pontieu, B, Carlsson, M, Vissers, G: 2009 *Astron. Astrophys.* **705**, 272
- Ugarte-Urra, I, Warren, H.P: 2011 *Astrophys. J.* **730**, 37.
- Verwichte, E, Marsh, M, Foullon, C, Van Doorselaere, T, De Moortel, I, Hood, A.W, Nakariakov, V.M: 2010 *Astrophys. J. Lett.* **724**, L194.

- Wang, T.J, Ofman, L, Davila, J.M: 2009 B. Lites, M. Cheung, T. Magara, J. Mariska, and K. Reeves(eds.) *The Second Hinode Science Meeting: Beyond Discovery-Toward Understanding. Boulder Colorado* **415**, 28.
- Warren, H.P, Ugarte-Urra, I, Young, P.R, Stenborg, G: 2011 *Astrophys. J.* **727**, 58.
- Young, P.R., O'Dwyer, B., Mason, H.E: 2012 *Astrophys. J.* **744**, 14.
- Yuan, D, Nakariakov, V: 2012 *Astron. Astrophys.* , in press